ISSN 2320 - 2599
Volume 7, No. 1, January – February 2018
International Journal of Microwaves Applications
Available Online at http://www.warse.org/IJMA/static/pdf/file/ijma01712018.pdf
https://doi.org/ 10.30534/ijma/2018/01712018

Microwave Nondestructive Testing of Galvanic Corrosion and Impact Damage in Carbon Fiber Reinforced Polymer Composites

Ram M. Narayanan[1], Robin James[2]
[1]The Pennsylvania State University, USA, rmn12@psu.edu
[2]The Pennsylvania State University, USA, rzj126@psu.edu

ABSTRACT

Advanced composite materials are being used extensively in many commercial and military aircraft and rotorcraft due to their superior stiffness and high strength-to-weight ratio. These composites are subjected to unexpected environmentally assisted damages. This work covers exploration and the methodology of detection of two such types of damages - galvanic corrosion and impact damages, at the earliest stages of development.

When aluminum alloy and CFRP are coupled together, the structural strength of the aircraft is unparalleled, but this comes at a price, namely galvanic corrosion (GC). Previous experimental results have shown that when CFRP composite materials are joined with high strength aluminum alloys, galvanic corrosion occurs at the material interfaces, and the aluminum is in great danger of corroding.

Composite materials used in aircraft are often subjected to unexpected environmental impact loads at high speeds, such as bird strikes and hailstone impacts. The damages developed in such cases is primarily in the form of delamination and matrix cracking, known as barely visible impact damage (BVID), since they are not easily observable by the naked eye. Prediction and detection of such environmental damages, which can occur in the service life of the aircraft, are of paramount importance in the aerospace industry.

This work utilizes the software BEASY for the prediction of galvanic corrosion and utilizes ABAQUS Explicit for modeling the bird impact damage and the hailstone impact damage by using the smoothed particle hydrodynamics (SPH) modeling method. This work also proposes a non-invasive microwave nondestructive testing (NDT) technique that can be employed as a detection methodology to detect the aforementioned types of environmentally assisted damages. Radar signals operating at a set frequency range can be used to detect the aforementioned environmentally assisted damages to obtain high-resolution 2D images of such damages.

Key words: aircraft structures, composites, galvanic corrosion, impact damage, nondestructive testing.

This work was sponsored by the U.S. Office of Naval Research under grant number N00014-15-1-2021.

1. INTRODUCTION AND MOTIVATION

In the aviation industry, composite materials are becoming increasingly imperative in the construction and manufacturing of aerospace structures both for commercial and military applications due to their light weight and good specific strength. In order to increase the fuel efficiency of aircrafts, greater dependence has been imposed upon light weight composite materials, such as carbon fiber reinforced polymer (CFRP) and glass fiber reinforced polymer (GFRP), apart from aluminum, titanium and magnesium. In many aircraft primary and secondary structures, composites may be attached to metals using metallic fasteners and rivets due to the structural requirements to be achieved in the design. One such scenario is the coupling of CFRP plate with aluminum alloy AA2024-T3 using stainless steel SS-304 bolts and nuts, which is investigated in Section 2 of this paper.

Previous work has demonstrated experimentally how corrosion occurs between graphite/polymer composite materials and some particular metals, such as 2014 aluminum, pure grade titanium, 316 stainless steel and monel, when the respective couples are exposed to corrosive environments in natural seawater [1]. Computational models have been developed and validated to simulate galvanic corrosion in aircraft environments between CFRP and AA2024 co-planar bimetallic pairs [2]–[5]. Electrochemical corrosion performance and environmentally induced mechanical degradation of aerospace epoxy adhesives with carbon nanotubes (CNTs) additives have been studied [6]. Detection methodologies employed before have not specifically explored precursors of corrosion growth to assess the aircraft's structural life and structural life extension [7]–[12]. NDT technologies have also been developed for the inspection of cracking and corrosion under coatings [13]. The rapid, reliable, and robust determination of structural and material flaws caused by material degradation and corrosion are very essential for maintaining the integrity and proper exploitation of military aircrafts. Corrosion control is the single most important preventive measure that can be taken to combat degradation of the fleet's aircraft, support equipment, and control costs [14].

In recent years, CFRP and GFRP composites have begun to be used in outer layers of the commercial as well as military

aircraft and must survive the most extreme of environmental conditions during service. On several occasions, these aircraft experience environmentally induced high-speed impact loads such as bird strikes and hailstone hits, which cause severe damage impairing structural integrity and causing catastrophic consequences. Sometimes, these bird strikes and hailstone impact loads can lead to BVID developing within the inner layers of the composite laminate which can be impervious to detection at the earliest stages of development, especially if the damage is not apparent at the outer surface of the aircraft. It is widely known that CFRP laminates are more vulnerable to undergo deformation when they are struck with an impact load which tends to damage their structural integrity, thereby greatly diminishing their mechanical properties [15]–[18]. The carbon fibers in the CFRP laminate have a very low capacity to absorb the impact energy as compared to other fibers such as aramid fibers and glass fibers. This is the reason GFRP and aramid fiber reinforced polymers show better resistance to impact loading. Previous work has shown a methodology of improving the impact resistance of CFRP laminates using comingled yarn fibers [19]. The idea of adding small weight of glass and aramid fibers to the CFRP laminate was proposed to improve the impact response of the hybrid composite material [20]. This hybrid method enhances the impact response of the structural component but results in increasing the overall weight of the structural component. When these CFRP laminates undergo impact loading, it becomes increasingly imperative to characterize the damage.

There are various NDT methods to characterize the galvanic corrosion as well as impact damage. Ultrasonic NDT methods are the most common methods to analyze composite structures [21] and have evolved into structural health monitoring systems for real time detection of defects in composites. Additionally, several other types of post impact NDT techniques such as X-ray, optical, Scanning Electron Microscopy (SEM) and infrared thermography could be employed to assess how the damage is propagating. SEM and optical methods only detect surface damages and are not able to see beneath the surface into the areas in between different layers of the CFRP laminate to detect fiber cracking and delaminations. A structural health monitoring system was developed for the purposes of damage identification using a pitch-catch approach to detect a low velocity impact damage on an aircraft winglet structure [22]. In recent years, microwave NDT techniques have been employed to detect dielectric changes in the form of damages in aircraft structures and have become increasingly effective in producing multiresolution images of defects in a non-invasive, non-contact scheme. A microwave scanning technique for inspecting the structural integrity of glass fiber T-joints in wind turbine blades was introduced which was able to simulate impact damage detection in aerospace composites by using near-field microwave waveguide imaging [23], [24].

This paper addresses two objectives. The first is to look at the behavior of an electrochemical system used in naval aircraft structures comprising of three components i.e. CFRP plate, SS-304 bolts and nuts, and AA 2024-T3 plate using the BEASY galvanic corrosion software. Our simulation results show how the corrosion progresses in a 3.5% salt solution (typical marine environment) around the boundary of the bolts and nuts of different sizes and how the potential, current density, corrosion rate and the mass loss changes with increasing corrosion. This is investigated in Section 2 of this paper.

In addition, Section 3 demonstrates low velocity bird strike and hailstone impact simulations have been conducted on an eight-layer unidirectional CFRP laminate, to characterize the impact response of the laminate after the impact has occurred.

In Section 4, a microwave NDT technique in the X-band microwave frequency range (8–12 GHz) is proposed to effectively detect the presence of corrosion products and impact damage. Results show that X-band radar signals can detect and image corrosion regions and BVID occurring on the metal plate behind the CFRP laminate.

This paper significantly expands on earlier versions of our work published recently [25], [26] and provides new results and additional theoretical considerations.

2. THEORY OF GALVANIC CORROSION

The phenomenon of galvanic corrosion is one of the most frequently occurring types of corrosion that results when a metal (aluminum, in this case) is in contact with another conducting material (CFRP, in this case) in a corrosive environment.

When two dissimilar conducting materials (i.e. at opposite ends of the galvanic series) in electrical contact with each other are exposed to an electrolyte, a current, called the galvanic current, flows from one to the other. Galvanic corrosion is that part of the corrosion that occurs at the anodic member of such a couple and is directly related to the galvanic current by Faraday's law [27]. The galvanic current generated causes a reduction in the total corrosion rate of the cathodic member of the couple.

In the current scenario, the aluminum (less noble) acts as the anode and the carbon fiber (more noble) in the CFRP acts as the cathode. The anode is the conducting material which has a lower (more negative) electrode potential than the cathode in the galvanic series. The electrochemical setup of the aluminum and the CFRP plate with the electrolyte penetration in the interface of the couple is shown in Figure 1.

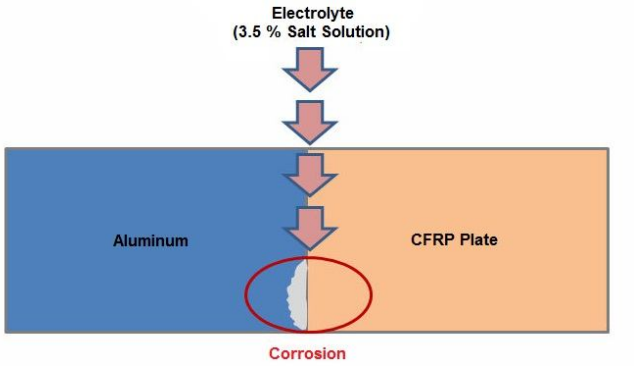

Figure 1: The galvanic couple of aluminum and CFRP showing the formation of corrosion

2.1 Mathematical Theory of Galvanic Corrosion

The agenda of the mathematical model is to study the thin-film electrolyte conditions that may appear in the upper part of the aircraft structure. The mathematical model includes a 3D finite element method that is used to solve the current density and electric potential in the electrolyte and at the anode (AA2024) and cathode (CFRP) surfaces. This model can be used with the experimental /simulation data to characterize the corrosion growth between the galvanic couple. The potential distribution within the electrolyte of a galvanic system is based on the continuity equation for conservation of charge (q) in the electrolyte under steady state conditions, and is given by [28]

$$\vec{\nabla} \cdot \mathbf{i} = \partial q / \partial t \,, \tag{1}$$

where $\mathbf{i}$ is the current density.

A steady state electrochemical system is one in which the charge remains constant, namely $\partial q / \partial t = 0$. Thus, $\vec{\nabla} \cdot \mathbf{i} = 0$.

The relationship between the electric field intensity $\mathbf{E}_e$ and the electric potential ϕ_e of the electrolyte is given by [28]

$$\mathbf{E}_e = -\vec{\nabla} \cdot \phi_e \,. \tag{2}$$

Ohm's Law is given by

$$\mathbf{i} = \sigma \mathbf{E}_e = -\sigma \vec{\nabla} \cdot \phi_e \,, \tag{3}$$

where σ is the conductivity of the electrolyte. The domain of integration ω of this 3D problem is the electrolyte, and the boundaries $\tau = \partial\omega$ are given by all the surfaces surrounding the electrolyte, i.e. the anode (AA2024), the cathode (CFRP) and the SS-304 bolts and nuts. The boundary condition applied to the CFRP and the AA2024 is of the form [2]

$$\mathbf{i}_n = -\sigma \, \partial \mathbf{E}_e / \partial \hat{n} = f(\Delta\phi) \,, \tag{4}$$

where $\mathbf{i}_n$ is the current density flowing throughout the surface of the specimen in a direction normal to the surface of the specimen $\hat{n}$, f is a non-linear function, and $\Delta\phi$ is the polarization potential across the interface of the metal (AA2024 or CFRP) and the electrolyte [2], given by

$$\Delta\phi = \phi_e - \phi_m \,, \tag{5}$$

where ϕ_m is the potential of the material (AA2024 or CFRP).

The thin-film electrolyte module of the BEASY Corrosion Manager, used for the simulations, needs the polarization data as input to provide the non-linear boundary condition to the anode and the cathode. In the thin-film electrolyte model used here, all the surfaces that are in contact with the thin layer of electrolyte apart from the interfaces with the AA2024 and the CFRP plates are considered as insulating. Therefore, at all those surfaces, we have $\mathbf{i}_n = 0$.

We know that the electrolyte thickness t_e is very small (of the order of microns) and therefore can be considered negligible compared to its other dimensions. Therefore, the problem reduces to one where we can employ a 2D approach since the electric potential and current density remain constant along the thickness coordinate.

In the 2D approach, the variables along the thickness coordinate are excluded from the mathematical formulation [2], thus reducing the electro-neutrality equation $\vec{\nabla} \cdot \mathbf{i} = 0$ to

$$t_e \vec{\nabla} \cdot (-\sigma \vec{\nabla} \phi_e) = -i_n(\Delta\phi) \,, \tag{6}$$

where $i_n(\Delta\phi)$ is the magnitude of the current density from the anode (AA2024) and the cathode (CFRP), which is zero for any insulating surface, and the del operator is two dimensional. The modeling approach used here to solve (6) is based on the finite element method (FEM).

2.2 Simulations using BEASY

BEASY Corrosion Manager is a software package that provides a rapid assessment of the risks to structural members in an aircraft that have chances of undergoing corrosion, especially areas where there are dissimilar metals joined together or carbon based composites (e.g. CFRP) are joined to other metals [29]. The approach used to model the corrosion is very similar to that used in structural analysis where the computer-aided design (CAD) model of a structure, which is supposed to be analyzed, is divided into finite elements. Environmental conditions around the structure near the corrosive electrolyte can be given as input parameters to identify the potential corrosion sites and the extent of corrosion occurring in those locations.

To conduct the simulation in BEASY Corrosion Manager, it is imperative to first create a CAD model of the specimen which

consists of an aluminum 2024 plate (0.02″ thick) coupled to a twill weave CFRP plate (0.045″ thick) via SS-304 bolts and nuts of dimensions 1/4″, 5/16″, 3/8”, 7/16″ and 1/2″. The original specimen and the CAD model are shown in Figures 2(a) and 2(b) respectively.

(a)

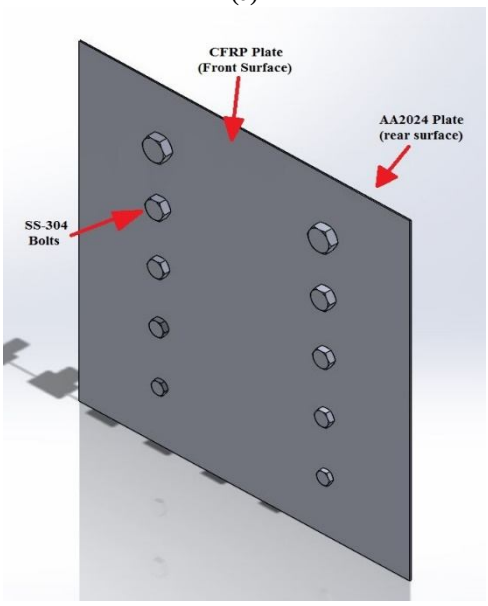

(b)

Figure 2: (a) Original Specimen, and (b) CAD model used for the analysis of the galvanic couple

A section of the CAD model designed is imported into BEASY Corrosion Manager along with the polarization data for the various materials in the assembly (AA2024, SS-304, and CFRP). Specific environmental parameters must be taken into consideration before running the simulation in BEASY. The electrolyte conductivity was assumed to be 5.58 S/m, which approximates a 3.5% NaCl solution. The film thickness of the electrolyte was considered to be 1000 μm.

Symmetry of the CAD model is used for the analysis and the results obtained are displayed. The potential distribution is shown in Figure 3(a) for the CFRP surface and in Figure 3(b) for the AA2024 surface. We can also observe how the potential (in Volts) varies according to the size of the SS-304 bolts used.

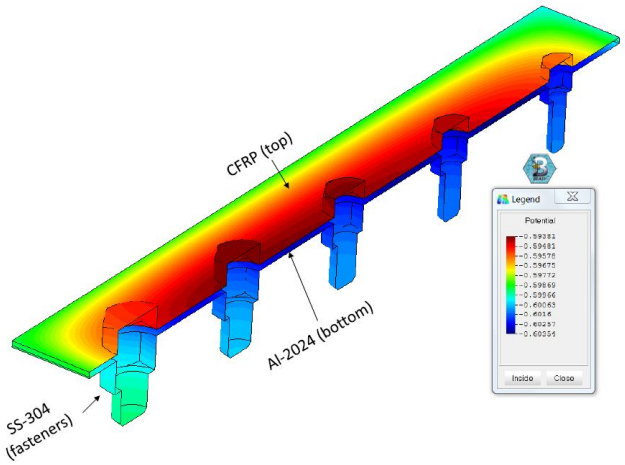

(a)

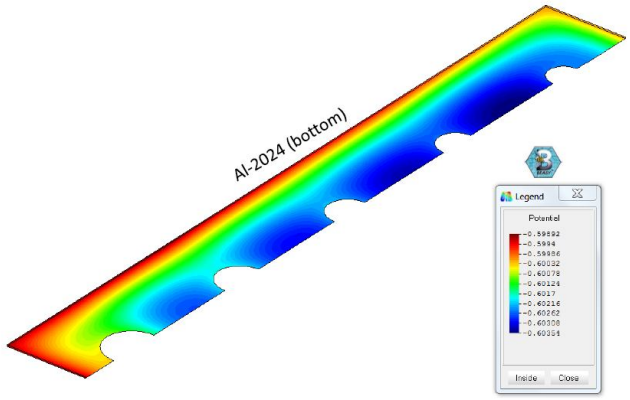

(b)

Figure 3: Potential distribution (in V) at the (a) CFRP surface, and (b) AA2024 surface

The current density of the anode (AA2024) changes with the progression of corrosion. The current density of the cathode (CFRP) remains constant because the CFRP does not corrode but instead undergoes cathodic protection. Figures 4(a) and 4(b) show the distribution of current density (in A/m^2) on the CFRP surface and on the AA2024 surface of the specimen, respectively.

The distribution of corrosion rate (mm/year) is shown in Figure 5 and the distribution of mass loss rate ($g\ m^{-2}\ day^{-1}$) of the anode is shown in Figure 6.

The simulation results clearly portray how the distribution of the various electrochemical parameters for a set of given environmental conditions change within the specimen as the distance from the fasteners increases. The effect of fastener sizes used in the specimen is also observed around the periphery of the fasteners from these contour plots.

Keeping in mind our detection strategy, which is based on obtaining the dielectric properties of the corrosion products for a given set of environmental conditions, we can create similar contour plots and derive an empirical relationship between the electrochemical parameters and the dielectric properties of the corrosion products and the overall specimen.

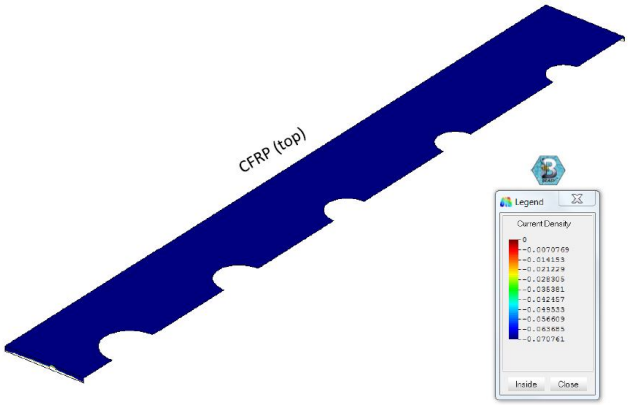

(a)

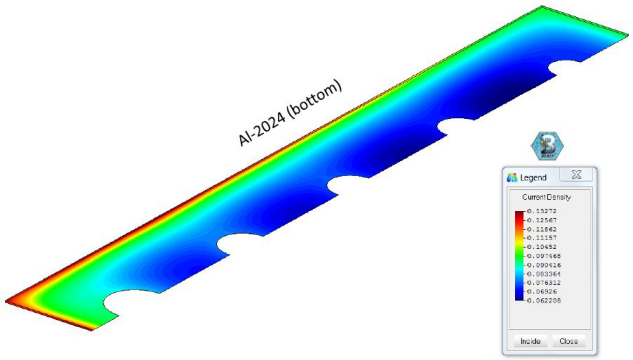

(b)

Figure 4: Current density distribution in A/m^2 at the (a) CFRP surface, and (b) AA2024 surface

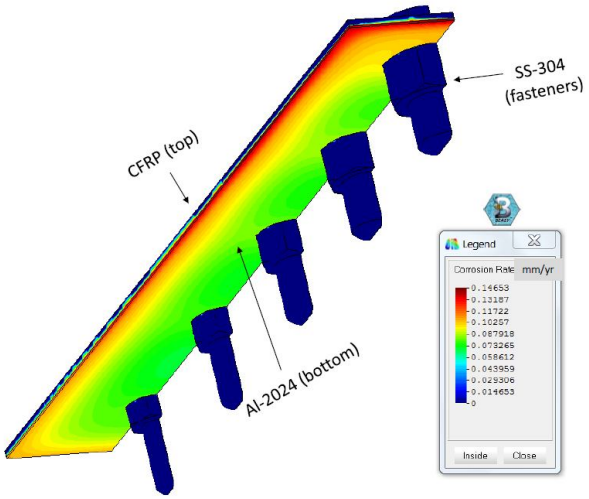

Figure 5: Corrosion rate on the AA2024 surface of the specimen (in mm/year)

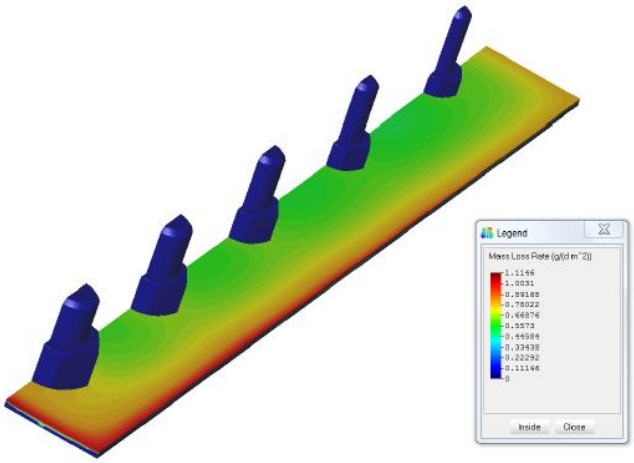

Figure 6: Mass loss rate on the AA2024 surface of the specimen (in g m^{-2} day^{-1})

2.2 Chemistry of Galvanic Corrosion

To understand how a microwave NDT technique would work, we characterize the corrosion process occurring at the anode and the cathode keeping in mind the chemical reactions that take place. At the anode, aluminum loses electrons to form Al^{3+} ions. These electrons will move towards the cathode where they will recombine with ions (mostly hydrogen ions) from the electrolyte and give off hydrogen molecules. The aluminum ions dissolve into the electrolyte, and deposit collects on the CFRP plate. The carbon fiber in the CFRP plate is nobler than the aluminum and therefore it is protected.

We first consider the chemical reaction of the salt dissolving in water to form the salt solution, resulting in the formation of hydrochloric acid and sodium hydroxide, given by

$$NaCl + H2O \rightarrow HCl + NaOH. \quad (7)$$

The hydrochloric acid in the electrolyte will give off hydrogen ions and chloride ions, as shown below:

$$HCl \rightarrow H^{+} + Cl^{-}. \quad (8)$$

Now, the aluminum ions formed earlier combine with the chloride ions to form aluminum chloride, as shown below:

$$Al^{3+} + 3Cl^{-} \rightarrow Al(Cl)_3 + 3e^{-}. \quad (9)$$

The formed aluminum chloride reacts with the water molecules in the aqueous salt solution to form aluminum hydroxide, as shown below:

$$Al(Cl)_3 + 3H_2O \rightarrow Al(OH)_3 + 3HCl. \quad (10)$$

From (9), it is clear that the end product of corrosion process between aluminum and CFRP formed on the surface of the aluminum is aluminum hydroxide. However, it is important to notice from (8) that an intermediate substance, i.e. aluminum

chloride, is formed. At the cathode, additionally, the following reaction takes place in which the sodium ions from the salt react with water molecules in the presence of oxygen to form sodium hydroxide [30], given by

$$4e^- + O_2^+ + 4Na^+ \rightarrow 4NaOH. \quad (11)$$

The proposed microwave NDT approach to corrosion detection is based on detecting the presence of aluminum hydroxide at the CFRP-Al interface, using the dielectric constant contrast between it and the CFRP material. Measurements indicate that at 12 GHz, the complex dielectric constant of aluminum hydroxide is about 2.5 [31] while that of CFRP is about $10 - j10$ when the electric field is oriented perpendicular to the fiber direction (to achieve high signal penetration) [32]. Thus, there is adequate dielectric constant between the CFRP material and the aluminum hydroxide to appear as differences in the image. Moreover, the skin depth in the CFRP is computed as 5.62 mm, which is the value where the incident power drops off to a value of $1/e^2$ or 13.5%.

3. SOFT BODY IMPACT DAMAGE IN COMPOSITES

When aircrafts operate at high altitudes, they can be subjected to conditions such as flying through a hailstorm or a flock of birds, which can be extremely dangerous to their structural integrity. The impact that can occur due to the hailstones and birds of various sizes at a cruise velocity can lead to serious consequences. Leading edges of wings and tail surfaces, the rudders, the engine and engine pylons, the pilot's windscreen, and the radome of the aircraft are some of the parts that are most threatened by such impacts.

These hailstone and bird impacts may not result in a collapse of the structure of the aircraft but can lead to invisible or BVID and may cause significant delaminations in the lower layers of the composite materials being used in the aircraft. These delaminations are not easily detected and may cause serious accidents if not attended to. Therefore, it is extremely important to predict the amount of damage caused by a hailstone impact or a bird impact. These impact types mentioned are likely to cause stress concentrations in the inter-ply regions of composite laminates where large differences in stiffness exist.

During the impact, the impactor (hailstones or bird) itself undergoes finite deformations and transitions from a solid to a semi-solid and finally to a liquid state. Hence, these impacts are termed as soft body impacts. The most popular methods of simulating soft body impact damage on composite laminates is the Smoothed Particle Hydrodynamics (SPH) Method.

Simulations are performed based on the SPH model which is appropriate for soft body impacts wherein the impactor is highly deformed or fragmented into a debris cloud on impact. In this model, a gridless, meshless Lagrangian technique is used in which the solid finite element mesh is replaced by a set of discrete interacting particles. Thus, the impactor material is considered as a set of discrete particles (nodes) that are independent from each other.

3.1 Smoothed Particle Hydrodynamics (SPH) Method

A brief review of the SPH method is provided in this sub-section for the sake of completeness and better understanding of our simulations. The SPH method can be considered as a finely meshed structure with solid elements where the elements themselves are discarded and only the nodes are kept [33]. The connectivity between the nodes only depends on the proximity of the neighboring nodes, called particles. All information such as stress, displacement, mass and density are computed at each node by including the contribution of each neighboring particle based on its proximity to each given neighbor.

For soft body impacts, the polynomial model for the equation of state (EOS) for the pressure p is of the form [34]

$$p = C_0 + C_1\mu + C_2\mu^2 + C_3\mu^3, \quad (12)$$

where $C_i, i = 0,1,2,3$ are materials constants and μ is a dimensionless parameter, defined as

$$\mu = (\rho/\rho_0) - 1, \quad (13)$$

where ρ and ρ_0 are the densities of the impactor its current (deformed) and initial (undeformed) states, respectively.

For small and moderate values of μ, it has been shown that

$$C_1 = \rho_0 c_0^2, \quad (14)$$

$$C_2 = (2k-1)C_1, \quad (15)$$

$$C_3 = (k-1)(3k-1)C_1, \quad (16)$$

where k is a materials constant and c_0 is the speed of sound in the material. The initial equilibrium pressure in the impactor, C_0, is assumed to be negligible, and C_1 is recognized as the bulk modulus of the impactor.

Alternatively, the simpler Murnaghan EOS model for the pressure p is of the form [35]

$$p = p_o + C_1\left[\left(\frac{\rho}{\rho_0}\right)^7 - 1\right]. \quad (17)$$

For a homogenized soft body, such as a bird, of porosity denoted as α, the EOS is written as [36]

$$\frac{\rho_0}{\rho} = (1-\alpha)\left(\frac{p}{A}+1\right)^{-\frac{1}{B}} + \alpha\left(\frac{p}{p_0}\right)^{-\frac{1}{7}}, \quad (18)$$

where

$$A = \frac{\rho_0 c_0^2}{(4s-1)}, \quad (19)$$

$$B = 4s-1, \quad (20)$$

and s is the coefficient which relates impact and shock velocities.

More complex EOS models have also been developed. The choice of the EOS model depends on the individual software package used, as most commercial codes are limited to one or few of the EOS formulations. However, in all EOS models, certain material constants must be defined as they typically cannot be measured directly [37].

3.2 Modeling of CFRP Laminate

The simulations were performed for soft body impact on an eight-layer unidirectional CFRP square laminate of side 305 mm (12 in) and an overall thickness of 1.52 mm (0.06 in), with the fibers oriented along the *x*-direction, as per the convention in Figure 3. Each layer (lamina) of the laminate has a thickness of 0.19 mm (0.0075 in). The mechanical properties of the CFRP laminate are provided in Table 1.

Table 1: Mechanical properties of unidirectional CFRP laminate

Property	Symbol	Value	Units
Young's modulus 0°	E_1	135	Gpa
Young's modulus 90°	E_2	10	Gpa
In-plane shear modulus	G_{12}	5	Gpa
Major Poisson's ratio	υ_{12}	0.3	
Ultimate tensile strength 0°	X_t	1500	Mpa
Ultimate compressive strength 0°	X_c	1200	Mpa
Ultimate tensile strength 90°	Y_t	50	Mpa
Ultimate compressive strength 90°	Y_c	250	Mpa
Ultimate in-plane shear strength	S	70	Mpa
Density	ρ	1.6	g/cm^3

Material properties given in Table 1 and geometry of the specimen defined above were used to model the unidirectional CFRP laminate. The Hashin-Rotem damage criterion [38] was selected for modeling as this one is already implemented in the Abaqus Explicit FEM code [39] used for the simulations.

The numerical models involved here have an explicit integration scheme to simulate the impact for a total of 5 ms. In this work, we developed a model using a homogenized shell, planar element, and then created a composite layup with the S4R conventional shell element. The S4R shell element has the following useful properties for our application: (1) uniformly reduced integration to avoid shear and membrane locking, (2) several hourglass modes that may propagate over the mesh, and (3) convergence to shear flexible theory for thick shells and classical theory for thin shells.

The CFRP laminate was partitioned into three distinct zones with the innermost zone (Zone 1) being the impact zone, and separated by the other two zones (Zone 2 and Zone 3) as illustrated in Figure 7(a). The CFRP laminate was meshed with the smallest element size in Zone 1 (2.5 × 2.5 mm^2) followed by Zone 2 (5 × 5 mm^2), and the largest element size in Zone 3 (10 × 10 mm^2) as illustrated in Figure 7(b). This was done in order to increase the computational efficiency of the model. The CFRP laminate was constrained in the translational degrees of freedom and was unconstrained in the rotational degrees of freedom for this simulation.

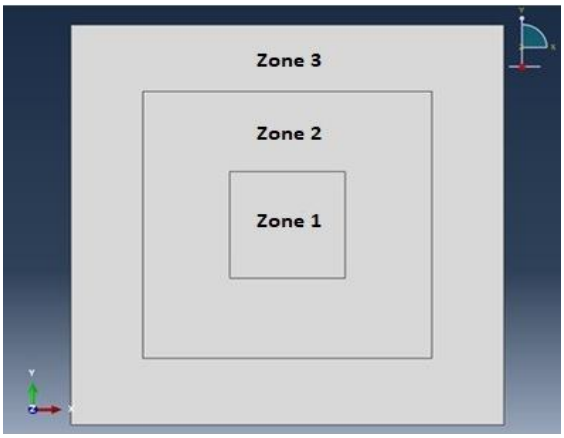

(a)

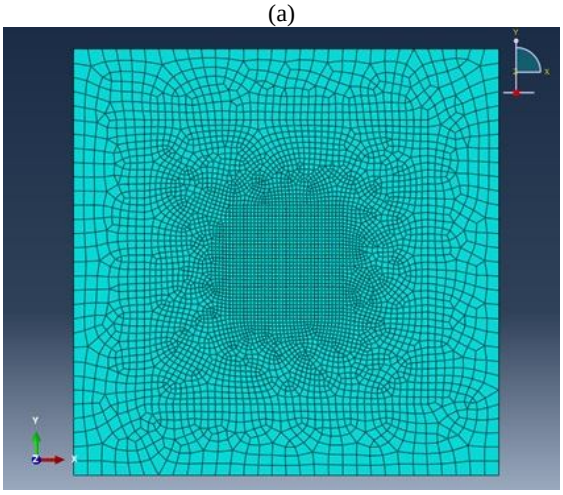

(b)

Figure 7: (a) CFRP laminate partitioned into distinct Zones with Zone 1 being the impact zone, and (b) Meshed model of the CFRP laminate

3.3 Simulation of Bird Impact Damage

The dependence of type and extent of deformation in a unidirectional composite plate as a function of the speed of bird strike impact was investigated [40]. For relatively low impact velocity (~75 m/s), the composite plate suffers global bending deformation due to the impact. However, when the impact velocity exceeds 125 m/s, the shear deformation is localized around the impact position. Thus, the damage characteristics in the composite significantly change from matrix-cracking to shear perforation as the impact velocity increases.

While a hard body impactor is often assumed to be a rigid body in impact analysis, a bird is a soft body impactor which exhibits considerable deformation during impact. These differences in impactor characteristics change the contact force history and the contact region [41]. A gelatin impactor, generally cylindrical in shape and matching the bird's dimensions, can be used as a model of an actual bird. Gelatin was found to possess the desired properties of a replica bird model since its equation of state (EOS) was similar to that of bird flesh on account of its high water content [42]. It has a non-porous density of 1.05–1.06 g/cm^3, which is very close to that of bird flesh. By increasing the porosity to 10% in order to take into account the voids and cavities in a real bird, its average density attains a value of about 0.95 g/cm^3, which is representative of the density of a real bird.

Thus, to simulate real bird impacts on structures, appropriate materials constants were used in the EOS representing a mixture of water with about 10% air, i.e. a porosity of 10%. The air content reduces the density and lowers the bulk modulus and speed of sound [43].

Based on a detailed survey of bird strike simulation papers and modeling data in technical literature, bird strike impact velocities used were mostly in the 100–250 m/s range and densities were in the 0.93–0.97 g/cm^3 range [37].

A. Bird Impact Simulation Setup

The bird impactor was modeled as a cylinder of length 178 mm (7 in) and diameter 32 mm (1.25 in). Its material properties used in the simulations are given in Table 2.

Table 2: Material properties of bird impactor

Property	Symbol	Value	Units
Young's modulus	E	5.3	GPa
Shear modulus	G	2	GPa
Poisson's ratio	υ	0.325	
Density	ρ	0.95	g/cm^3
Mass	m	136	g

The impactor (bird) was modeled as a meshless collection of particles as shown in Figure 8 using the SPH method and its equation of state (EOS) parameters were appropriately defined. The overall meshed model of the assembly is shown in Figure 9. This overall meshed model, initially has a meshed impactor whose nodes are used to discretize the impactor as a meshless collection of particles.

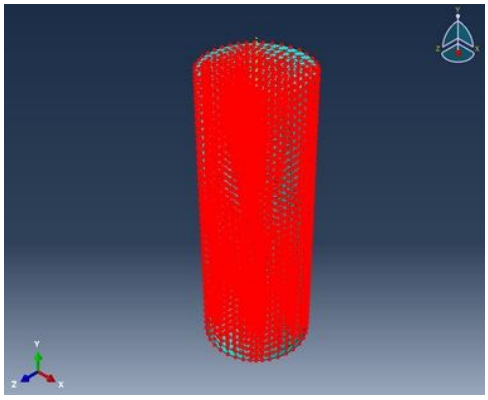

Figure 8: Bird impactor modeled as a meshless collection of particles

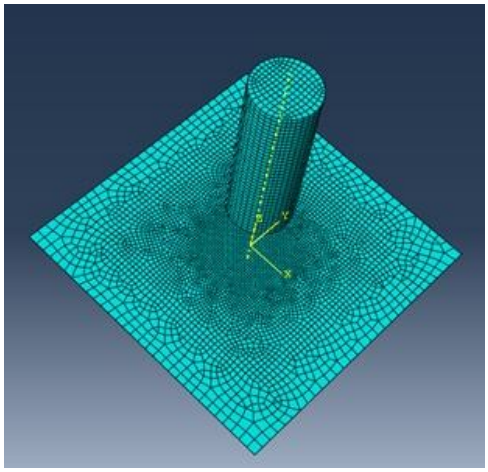

Figure 9: Overall meshed model of the overall assembly to be simulated in ABAQUS FEM code

B. Bird Impact Simulation Results

The simulation was conducted over a time period of 5 ms for an impactor velocity of 150 m/s hitting the topmost layer (Layer 1) of the unidirectional CFRP laminate. The impact energy is computed as 1530 J. The propagation time at which we assume that the effects of the impact are final is assumed to be 3 ms. Results of the impactor fragmentation are shown in Figure 10 at close to the start and end of the impact. Since the bird is a soft body, it breaks up quickly and its fragments are dispersed over the entire plate.

Displacements were obtained at the end of the propagation time period. Figure 11 shows the final displacement in the z-direction to be 7.47 mm (average value of the dark blue scale).

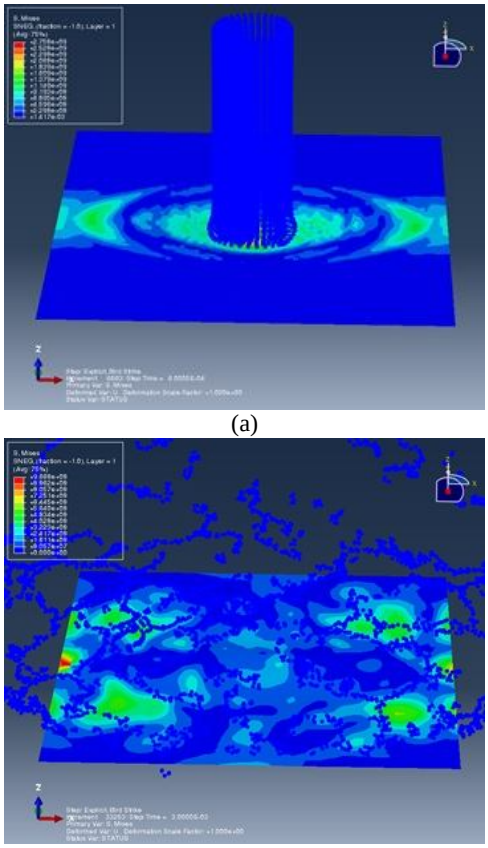

(a) (b)

Figure 10: Simulation results showing bird impactor fragmentation after impact at (a) 0.6 ms, and (b) 3.0 ms

3.4 Simulation of Hail Impact Damage

While the nominal density of fresh water ice is 0.917 g/cm^3, the average density of hail is 0.846 g/cm^3. However, large hailstones have a mean density close to that of pure ice [44] and have a polycrystalline structure with their mechanical properties depending on temperature and grain size. Hailstones can range in diameter from 0.5 cm to over 5 cm in more extreme cases; sizes greater that 2.5 cm (1 in) can inflict significant damage to structures [45].

Under compression and at high strain rates, ice material begins to behave in a more brittle manner with a more linear stress-strain curve and decrease in post-yield deformation [46]. Thus, it can be generally assumed that the behavior of hail is brittle upon impact [33].

A. Hailstone Impact Simulation Setup

The hailstone impactor was modeled as a sphere of diameter 32 mm (1.25 in). Its material properties used on the simulations are given in Table 3.

The impactor (hailstone) was also modeled as a meshless collection of particles as shown in Figure 12 using the SPH method and its equation of state (EOS) parameters were appropriately defined.

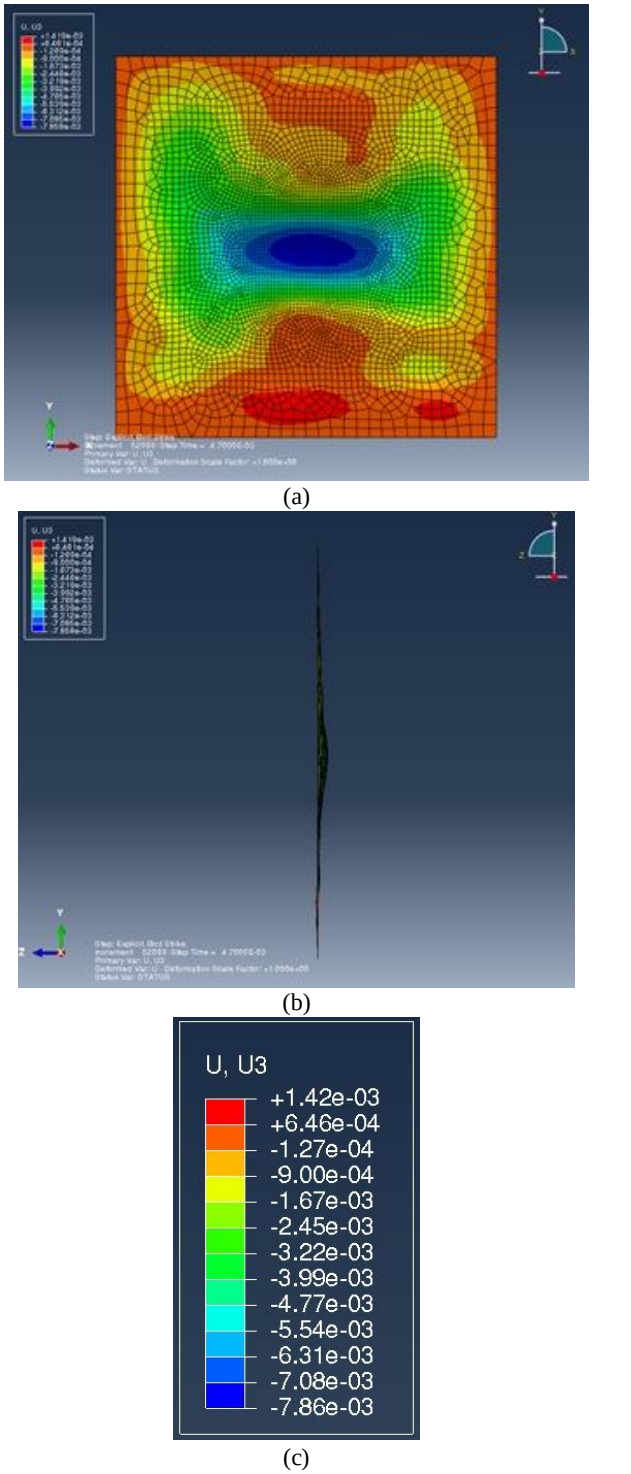

(a) (b) (c)

Figure 11: Bird impact results. (a) Front view of displacement, (b) Side view of displacement in the *z*-direction, and (c) Expanded color scale for side view of displacement

Table 3: Material properties of hailstone impactor

Property	Symbol	Value	Units
Young's modulus	E	9.33	GPa
Shear modulus	G	3.52	GPa
Poisson's ratio	υ	0.325	
Density	ρ	0.917	g/cm^3
Mass	m	15.7	g

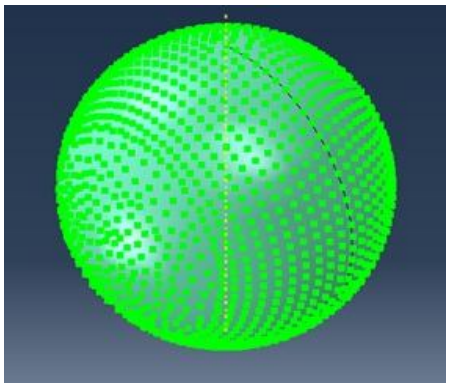

Figure 12: Hailstone impactor modeled as a meshless collection of particles

B. Hailstone Impact Simulation Results

The simulation was conducted over a time period of 5 ms for an impactor velocity of 150 m/s hitting the topmost layer (Layer 1) of the unidirectional CFRP laminate. The results of the impactor fragmentation are shown in Figure 13 near the start and at the end of the impact propagation time, which is assumed to be 3.1 ms. While the hailstone breaks up upon impact, its fragments are generally concentrated over the region of impact, namely Zone 1.

Displacements were obtained at the end of the propagation time period. Figure 14 shows the final displacement in the *z*-direction to be 7.58 mm (average value of the dark blue scale).

4. EXPERIMENTAL RESULTS

The approach for detecting the presence of the corrosion product (aluminum hydroxide) and impact damage (dents) on the surface of the aluminum alloy plate behind the CFRP composite laminate is based on the use of an X-band microwave NDT system. The X-band microwave frequency range (8–12 GHz) was chosen to achieve good wave penetration with high depth resolution to obtain multiresolution images. The X-band microwave NDT system was developed through which x-y raster scans of the test specimen could be conducted. The system consisted of an Agilent precision network analyzer (PNA) model N5225A to which a waveguide-to-coaxial adapter was connected. A short length of WR-90 rectangular waveguide section of inner dimensions 22.86 mm × 10.16 mm (0.9 in × 0.4 in) attached to the adapter acted as the antenna.

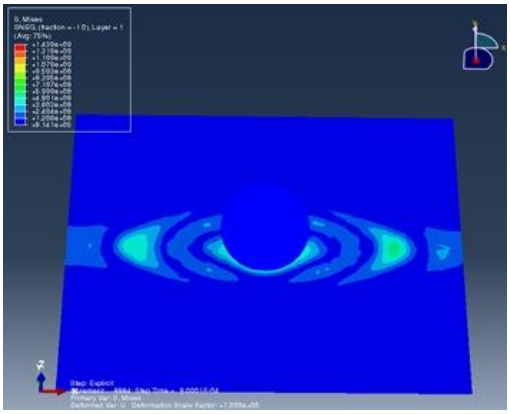

(a)

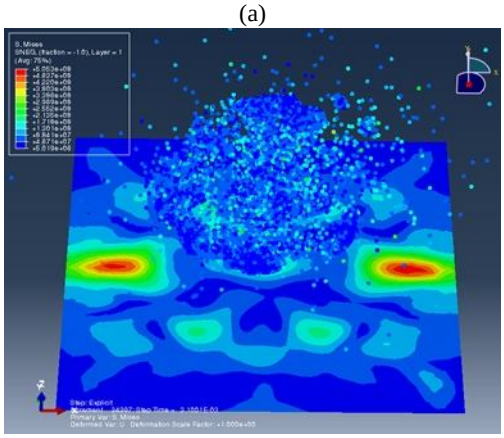

(b)

Figure 13: Simulation results showing hailstone impactor fragmentation after impact at (a) 0.8 ms, and (b) 3.1 ms

The adapter and waveguide section were mounted on the scanner and the coaxial port of the adapter was connected to the PNA using precision coaxial cables. Measurements were made of the input reflection coefficient. The measurement setup was calibrated using a metal plate as a calibration target, whose reflection coefficient was known to be −1. Best contrast in reflected powers was obtained for a standoff distance of 13 mm within a frequency range of 11.75–12 GHz. This frequency range and standoff distance were used to obtain the most enhanced images for the undamaged as well as damaged specimens for the impact damage propagation.

The block diagram of the experimental apparatus and a photograph of the test setup are shown in Figure 15. The specimens (materials under test) were prepared for testing and comparison. A reference sample was prepared where the aluminum alloy was joined to the unidirectional CFRP plate and without damage or defects. Next, damages were artificially induced and microwave images were obtained for the perfect reference sample as well as the damaged sample to render comparison.

The thickness of the CFRP panels used in our experimental study was 1.52 mm (0.06 in); thus, there was adequate signal penetration as the skin depth was earlier deduced as 5.62 mm in Section 2.2.

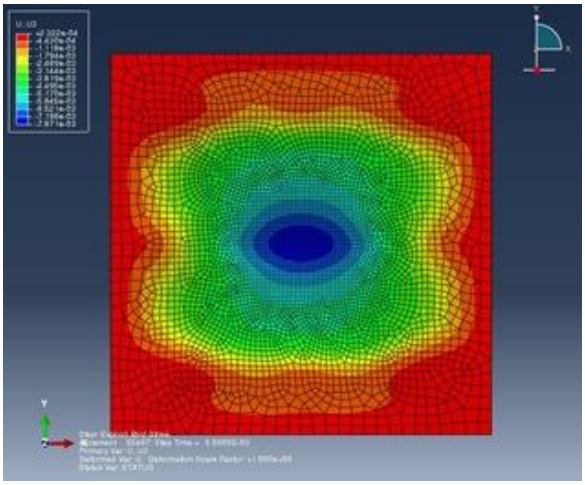

(a)

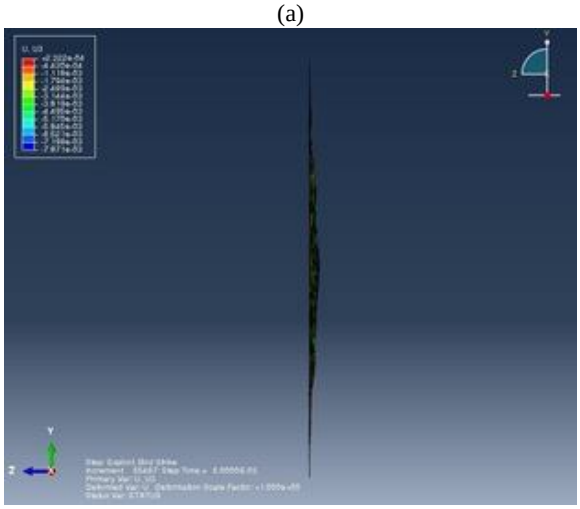

(b)

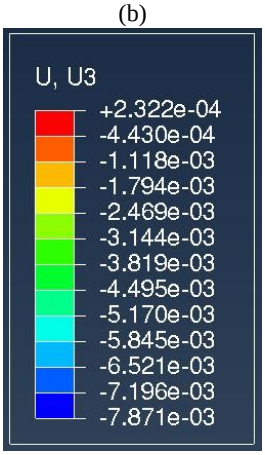

(c)

Figure 14: Hailstone impact results. (a) Front view of displacement, (b) Side view of displacement in the z-direction, and (c) Expanded color scale for side view of displacement

4.1 Galvanic Corrosion Detection

We conducted microwave imaging using the obtained standoff distance of 13 mm at a frequency of 11.95 GHz for the case of galvanic corrosion. Two scenarios were tested to simulate the presence of the galvanic corrosion product, aluminum hydroxide. The first scenario included imaging the CFRP plate alone (undamaged), and the CFRP plate with a Ziploc® bag containing aluminum hydroxide behind it (simulated corrosion). The second scenario consisted of using the aluminum alloy backing plate along with the CFRP and aluminum hydroxide. The aluminum hydroxide Ziploc® bags used for the tests are shown in Figure 16.

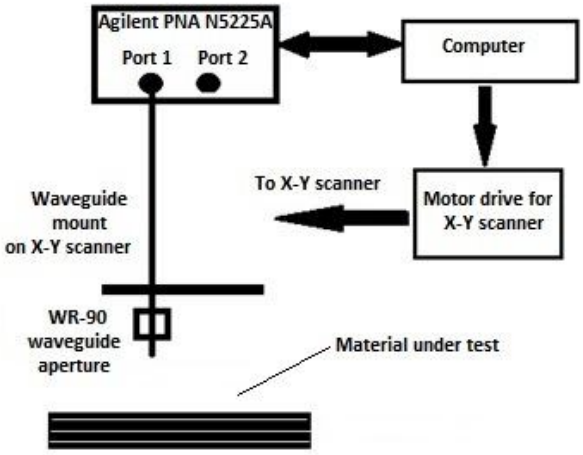

(a)

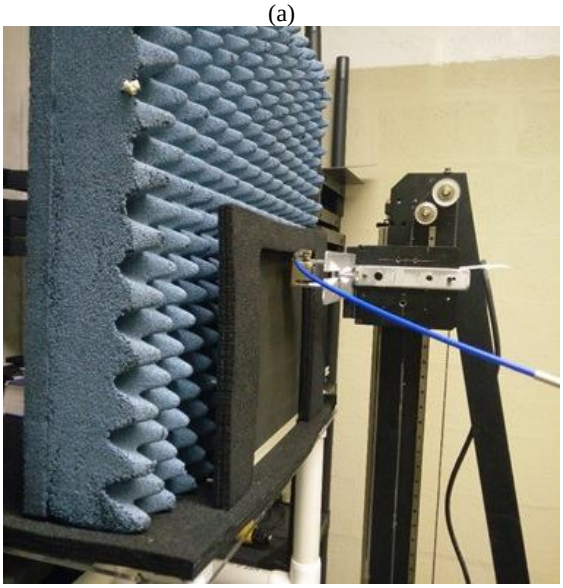

(b)

Figure 15: (a) Block diagram of X-band NDT system, and (b) Test setup

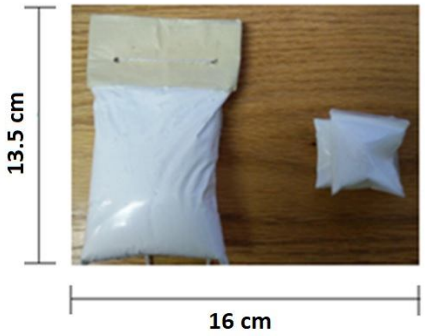

Figure 16: Ziploc® bags containing aluminum hydroxide: (Left) Thick bag of size 9×7×2 cm^3, and (Right) Thin bag of size 3.6×3.6×0.5 cm^3

In all images presented, the color scale represents values proportional to the reflected power from each specimen at each location. This allows us to compare images for different specimens.

In the first scenario depicting galvanic corrosion detection, microwave imaging was conducted using *x-y* raster scans on a CFRP plate, and then a thick bag of aluminum hydroxide was affixed behind the CFRP plate to simulate the presence of galvanic corrosion. The scanning area was kept as 10 cm × 10 cm and a frequency of 11.95 GHz was chosen. The obtained images are shown in Figure 17. In Figure 17(a), we can see that the top of the CFRP plate shows a higher reflection coefficient. This is because of the difference in the density of the carbon fibers in that region being higher than the remaining part of the CFRP plate. In Figure 17(b), we can clearly see the aluminum hydroxide being detected behind the CFRP plate, which is the region that has the higher reflection coefficient. The corrosion area is within the red oval in Figure 17(b).

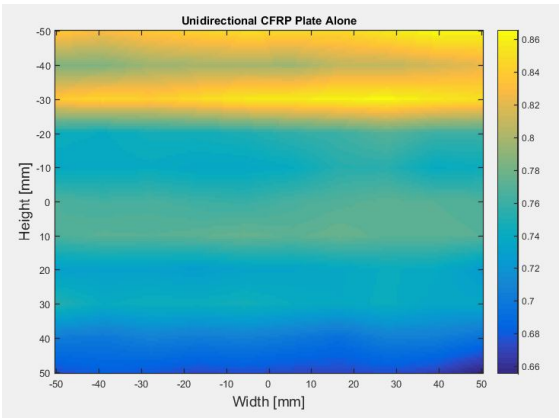

(a)

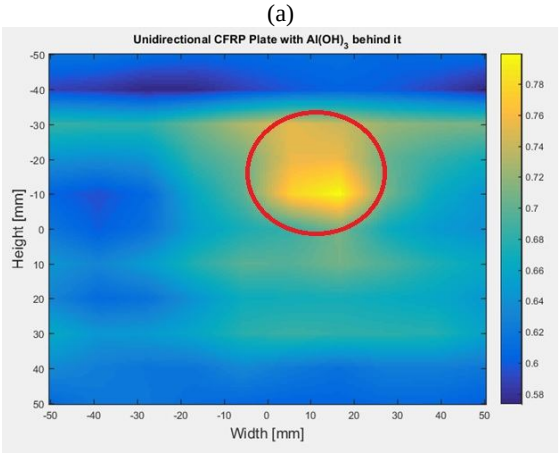

(b)

Figure 17: (a) Microwave image of CFRP plate, and (b) Microwave image of CFRP plate with aluminum hydroxide placed behind it

Next, we investigate a scenario wherein the thin sized Ziploc® bags containing aluminum hydroxide are sandwiched between the unidirectional CFRP plate and a dented aluminum alloy plate containing a cavity of extent 6.7 cm × 4.6 cm and depth 1.1 cm. The thin Ziploc® bags containing aluminum hydroxide was places inside this cavity.

Microwave imaging was conducted using *x-y* raster scans of the CFRP plate joined to the aluminum plate without any damage and was compared to the images obtained using the damaged specimen, where the dented aluminum cavity was empty first and was then filled with the thin aluminum hydroxide bag. Obtained images are shown in Figure 18. In Figure 18(b), the black oval depicts the position of the cavity and in Figure 18(c), the red oval depicts the corrosion area.

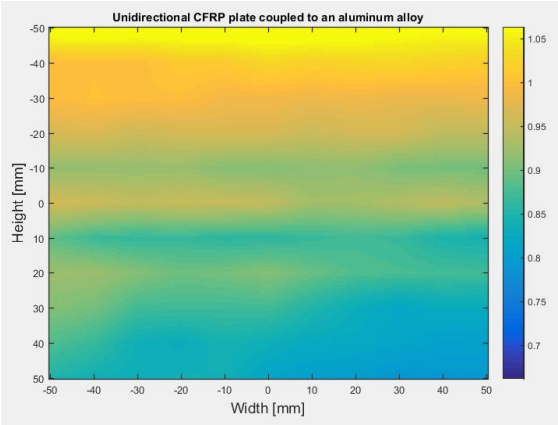

(a)

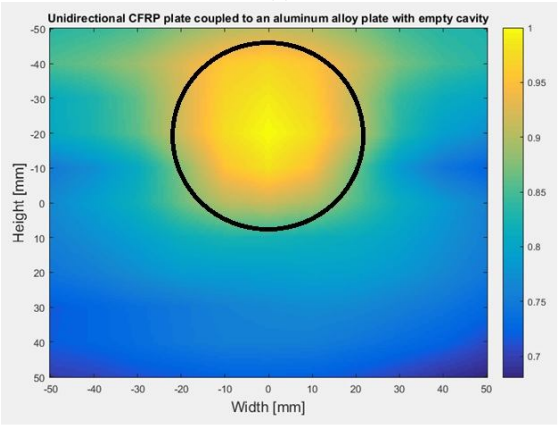

(b)

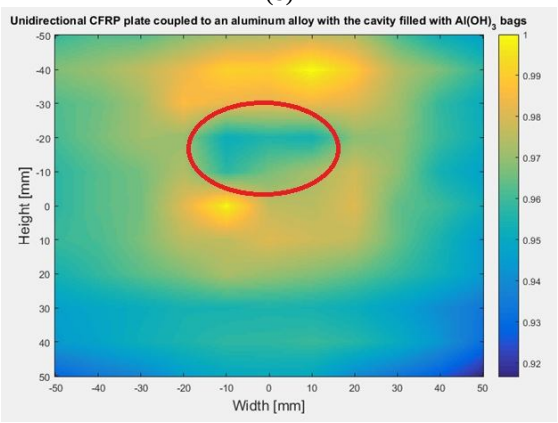

(c)

Figure 18: CFRP coupled to aluminum alloy with: (a) No damage, (b) Empty cavity, and (c) Cavity filled with a thin bag of aluminum hydroxide

In Figure 18, we can clearly see the difference in the images obtained at 12 GHz between the undamaged specimen, the damaged specimen with the empty cavity in the aluminum plate, and the damaged specimen with the aluminum cavity filled with aluminum hydroxide powder.

4.2 Impact Damage Detection

The impact energy in real-world scenarios discussed in the simulations presented in Section 3 is of the order of 70–1000 J. This value was too high to induce experimentally. We looked at the scenario of impact damage propagation onto an aluminum plate when the bi-material consisting of the CFRP laminate and aluminum alloy coupled together underwent impact damage on the CFRP surface from a tool drop. The tool (hammer) weighing 140 g was dropped from a height of 1.09 m on the CFRP surface, and the total impact energy was calculated as 1.5 J. It was felt that if this low-impact damage could be detected, then so could damage inflicted by impacts with greater energies, such as bird strikes and hailstone impacts. The impact caused by the tool drop created a BVID on the surface of the CFRP and also propagated through to cause a dent onto the aluminum alloy. The dent, which was about 3.6-cm long caused by the impact, is shown in Figure 19.

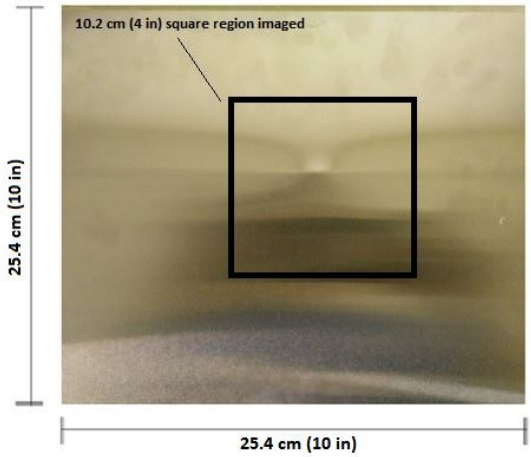

Figure 19: Dent appearing on the aluminum plate due to impact on the CFRP surface

Figures 20(a) and 20(b) show the X-band NDT scans of the undamaged and the damaged specimens, respectively, when viewed from the CFRP side. Figure 20(a) shows a relatively uniform pattern with high reflectivity owing to the presence of the flat aluminum plate viewed at normal incidence. When the structure is damaged due to the impact, the dent that forms in the aluminum is no longer flat, resulting in the scattering of the incident electromagnetic wave away from the normal owing to its crater-like shape. This phenomenon manifests itself as reduced reflectivity towards the antenna; thus, the dent region has lower reflectivity, which is easily observed in the image shown in Figure 20(b).

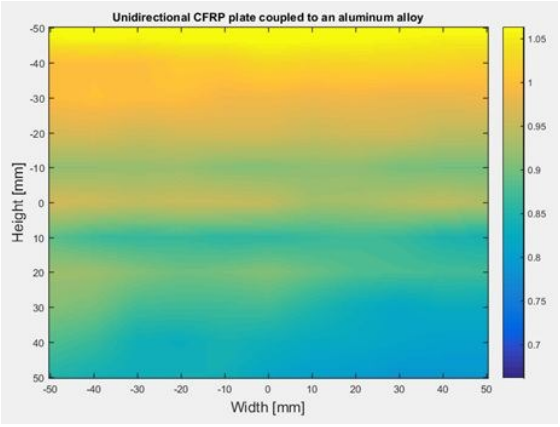

(a)

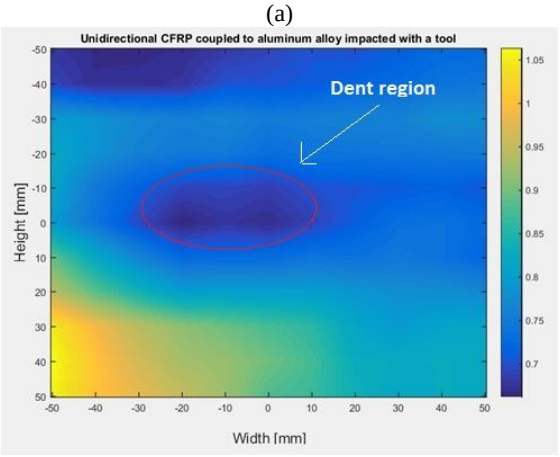

(b)

Figure 20: (a) NDT scan of undamaged specimen, and (b) NDT scan of impact damaged specimen

5. CONCLUSION

In this paper, we presented an approach for detecting defects occurring in typical CFRP-aluminum aircraft structures caused by galvanic corrosion and impact damage using microwave signals. The formation of such types of defects is discussed and strategies to detect these are presented. An experimental scanning X-band system is developed and used for generating images of several samples, pristine and containing simulated defects and damages. It is seen that X-band microwave signals are able to successfully image the damaged areas from standoff distances and therefore may be used for rapid low-cost non-invasive NDT of such types of aircraft structures.

ACKNOWLEDGEMENT

The assistance of Tae Hee Kim and Marc Navagato in the data acquisition and analysis is appreciated.

REFERENCES

1. W. C. Tucker, R. Brown, and L. Russell. **Corrosion between a graphite/polymer composite and metals**, *Journal of Composite Materials*, Vol. 24, pp. 92-102, January 1990. https://doi.org/10.1177/002199839002400105

2. S. Palani, T. Hack, A. Peratta, R. Adey, J. Baynham, and H. Lohner. **Modelling approach for galvanic corrosion protection of multi-material aircraft structures**, in *Proc. DoD Corrosion Conference 2011*, La Quinta, CA, USA, July-August 2011.
3. S. Palani, T. Hack, A. Peratta, R. Adey, J. Baynham, and H. Lohner. **Validation of a galvanic corrosion model for AA2024 and CFRP with localised coating damage**, in *Proc. 2010 European Corrosion Congress (Eurocorr 2010)*, Moscow, Russia, September 2010.
4. A. Peratta, T. Hack, R. Adey, S. Palani, J. Baynham, and H. Lohner. **Validation of a galvanic corrosion computer model for AA2024 and CFRP with localised coatings damage**, in *Proc. 2nd International Workshop on Light Weight Metal Corrosion & Modeling for Corrosion Prevention, Life Prediction and Assessment (CMLP 2010)*, Rome, Italy, April 2010.
5. A. Peratta, T. Hack, R. Adey, J. Baynham, and H. Lohner. **Galvanic corrosion modelling for aircraft environments**, in *Proc. 2009 European Corrosion Congress (Eurocorr 2009)*, Nice, France, September 2009.
6. G. Gkikas, A. Paipetis, A. Lekatou, N. M. Barkoula, D. Sioulas, B. Canflanca, and S. Florez. **Corrosion and environmental degradation of bonded composite repair**, *International Journal of Structural Integrity*, Vol. 4, pp. 67-77, 2013. https://doi.org/10.1108/17579861311303636
7. S. De, K. Gupta, R. J. Stanley, M. T. Ghasr, R. Zoughi, K. Doering, D. Van Aken, G. Steffes, M. O'Keefe, and D. Palmer. **A comprehensive multi-modal NDE data fusion approach for failure assessment in aircraft lap-joint mimics**, *IEEE Transactions on Instrumentation and Measurement*, Vol. 62, pp. 814-827, April 2013. https://doi.org/10.1109/TIM.2013.2240931
8. S. De, K. Gupta, R. J. Stanley, R. Zoughi, K. Doering, D. Van Aken, G. Steffes, M. O'Keefe, and D. Palmer. **A comprehensive structural analysis process for failure assessment in aircraft lap-joint mimics using intramodal fusion of eddy current data**, *Research in Nondestructive Evaluation*, Vol. 23, pp. 146-170, 2012. https://doi.org/10.1080/09349847.2012.660242
9. S. Kharkovsky, and R. Zoughi. **Microwave and millimeter wave nondestructive testing and evaluation – overview and recent advances**, *IEEE Instrumentation and Measurement Magazine*, Vol. 10, pp. 26-38, April 2007. https://doi.org/10.1109/MIM.2007.364985
10. J. S. Cargill, J. A. Pecina, S. M. Shepard, J. D. Weir, R. Zoughi, and A. V. Bray. **Nondestructive testing for corrosion under paint**, *Materials Evaluation*, Vol. 63, pp. 102-109, February 2005.
11. D. Hughes, N. Wang, T. Case, K. Donnell, R. Zoughi, R. Austin, and M. Novack. **Microwave nondestructive detection of corrosion under thin paint and primer in aluminum panels**, *Subsurface Sensing Technologies and Applications*, Vol. 2, pp. 435-471, October 2001. https://doi.org/10.1023/A:1013225219371
12. N. Qaddoumi, A. Shroyer, and R. Zoughi. **Microwave detection of rust under paint and composite laminates**, *Journal of Research in Nondestructive Evaluation*, Vol. 9, pp. 201-212, 1997. https://doi.org/10.1080/09349849709414474
13. K. G. Lipetzky, M. R. Novack, I. Perez, and W. R. Davis. **Development of innovative nondestructive evaluation technologies for the inspection of cracking and corrosion under coatings**, Naval Surface Warfare Center Carderock Division Technical Report NSWCCD-61-TR– 2001/21, November 2001.
14. Department of Navy. ***Annual Report on Corrosion for Fiscal Year 2016***, Washington, DC, USA: Department of Navy, 2016.
15. W. J. Cantwell and J. Morton. **The impact resistance of composite materials – a review**, *Composites*, Vol. 22, pp. 347-362, September 1991. https://doi.org/10.1016/0010-4361(91)90549-V
16. S. D. Bartus. **A review: Impact damage of composite materials**, *Journal of Advanced Materials*, Vol. 39, pp. 3-21, July 2007.
17. N. Razali, M. T. H. Sultan, F. Mustapha, N. Yidris, and M. R. Ishak. **Impact damage on composite structures – a review**, *International Journal of Engineering Science*, Vol. 3, pp. 8-20, 2014.
18. A. Ahmed and L. Wei. **The low-velocity impact damage resistance of the composite structures - a review**, *Reviews on Advanced Materials Science*, Vol. 40, pp. 127-145, 2015.
19. C. Thanomsilp and P. J. Hogg. **Penetration impact resistance of hybrid composites based on commingled yarn fabrics**, *Composites Science and Technology*, Vol. 63, pp. 467-482, February–March 2003. https://doi.org/10.1016/S0266-3538(02)00233-6
20. N. K. Naik and R. Ransimha. **Impact response and damage tolerance characteristics of glass carbon/epoxy hybrid composite plates**, *Composites Part B-Engineering*, Vol. 32, pp. 565-574, 2001. https://doi.org/10.1016/S1359-8368(01)00036-1
21. M. C. Bhardwaj and G. F. Stead. **Non-contact ultrasound: A new dimension for in and post-process analysis of materials**, in *Proc. 33rd International SAMPE Technical Conference*, Seattle, WA, USA, November 2001, pp. 46-57.
22. A. De Fenza, G. Petrone, R. Pecora, and M. Barile. **Post-impact damage detection on a winglet structure realized in composite material**, *Composite Structures*, Vol. 169, pp. 129-137, June 2017. https://doi.org/10.1016/j.compstruct.2016.10.004
23. Z. Li, A. Haigh, C. Soutis, A. Gibson, and R. Sloan. **Microwaves sensor for wind turbine blade inspection**, *Applied Composite Materials*, Vol. 24, pp. 495-512, April 2017. https://doi.org/10.1007/s10443-016-9545-9
24. Z. Li, A. D. Haigh, C. Soutis, and A. A. P. Gibson. **Simulation for the impact damage detection in composites by using the near-field microwave waveguide imaging**, in *Proc. 53rd Annual Conference of The British Institute of Non-Destructive Testing*, Manchester, UK, September 2014, pp. 66–75.
25. R. James, T. H. Kim, and R. M. Narayanan. **Prognostic investigation of galvanic corrosion precursors in**

aircraft structures and their detection strategy, in *Proc. SPIE Conference on Nondestructive Characterization and Monitoring of Advanced Materials, Aerospace, and Civil Infrastructure, and Transportation XI*, Portland, OR, USA, March 2017, pp. 101690C-1–101690C-12.

26. R. James, T. H. Kim, M. D. Navagato, and R. M. Narayanan. **Modeling and simulation of environmental impact damage of aerospace composites and its detection scheme**, in *Proc. 32nd American Society for Composites Technical Conference*, West Lafayette, IN, USA, Oct. 2017, pp. 2363-2377. https://doi.org/10.12783/asc2017/15355
27. X. G. Zhang. **Galvanic corrosion**, in *Uhlig's Corrosion Handbook*, R. W. Revie (ed.), Hoboken, NJ, USA: Wiley, pp. 123-143, 2011. https://doi.org/10.1002/9780470872864.ch10
28. J. W. Oldfield. **Electrochemical theory of galvanic corrosion**, in *Galvanic Corrosion*, H. P. Hack, (ed.), Philadelphia, PA, USA: American Society for Testing and Materials, pp. 5-22, 1988. https://doi.org/10.1520/STP26188S
29. BEASY. **BEASY galvanic corrosion case studies**, Available online: http://www.beasy.com/beasy/22-galvanic-corrosion.html , accessed on 4 April 2017.
30. E. Bosze and S. Nutt. **Potential for galvanic corrosion between carbon fibers and AL wires in ACCC/TW conductor**, University of Southern California Gill Foundation Composites Center Report, January 2008.
31. Vega. **List of dielectric constants**, Available online: https://www.vega.com/-/media/PDF-files/List_of_dielectric_constants_EN.ashx, accessed on 17 February 2018.
32. E. J. Riley. **Application of unidirectional carbon fiber reinforced polymer laminas in circuit-analog absorbers**, Ph.D. dissertation, Dept. Elect. Eng., Pennsylvania State Univ., University Park, PA, USA, 2018.
33. M.-A Lavoie, A. Gakwaya, M. J. Richard, D. Nandlall, D.; M. Nejad Ensan, and D. G. Zimcik. **Numerical and experimental modeling for bird and hail impacts on aircraft structure**, in *Proc. 28th International Modal Analysis Conference (IMAC-XXVIII)*, Jacksonville, FL, USA, February 2010, pp. 1403-1410.
34. A. F. Johnson and M. Holzapfel. **Modelling soft body impact on composite structures**, *Composite Structures*, Vol. 61, pp. 103-113, July-August 2003. https://doi.org/10.1016/S0263-8223(03)00033-3
35. T. Kermanidis, G. Labeas, M. Sunaric, and L. Ubels. **Development and validation of a novel bird strike resistant composite leading edge structure**, *Applied Composite Materials*, Vol. 12, pp. 327-353, November 2005. https://doi.org/10.1007/s10443-005-3441-z
36. D. Ivančević and I. Smojver. **Hybrid approach in bird strike damage prediction on aeronautical composite structures**, *Composite Structures*, Vol. 94, pp. 15-23, December 2011. https://doi.org/10.1016/j.compstruct.2011.07.028
37. S. Heimbs. **Computational methods for bird strike simulations: A review**, *Computers & Structures*, Vol. 89, pp. 2093-2112, December 2011. https://doi.org/10.1016/j.compstruc.2011.08.007
38. Z. Hashin and A. Rotem. **A fatigue failure criterion for fiber reinforced materials**, *Journal of Composite Materials*, Vol. 7, pp. 448-464, October 1973. https://doi.org/10.1177/002199837300700404
39. DS Simulia. **Abaqus 6.14 documentation**, Available online: http://abaqus.software.polimi.it/v6.14/index.html, accessed on 17 December 2017.
40. M. Nishikawa, K. Hemmib, and N. Takeda. **Finite-element simulation for modeling composite plates subjected to soft-body, high-velocity impact for application to bird-strike problem of composite fan blades**, *Composite Structures*, Vol. 93, pp. 1416-1423, April 2011. https://doi.org/10.1016/j.compstruct.2010.11.012
41. H. Morita and P. H. Wilson Tsang. **Soft body impact damage on CF/PEEK laminates using gelatin projectile**, *Journal of Reinforced Plastics and Composites*, Vol. 16, pp. 1330-1341, 1997.
42. J. S. Wilbeck and J. L. Rand. **The development of a substitute bird model**, *Journal of Engineering for Power*, Vol. 103, pp. 725-730, October 1981.
43. A.I. Khan, R. K. Kapania, and E. R. Johnson. **A review of soft body impact on composite structure**, in *Proc. 51st AIAA/ASME/ASCE/AHS/ASC Structures, Structural Dynamics, and Materials Conference*, Orlando, FL, USA, April 2010, Paper AIAA 2010-2865.
44. K. A. Browning, F. H. Ludlam, and W. C. Macklin. **The Density and Structure of Hailstones**, Imperial College of Science & Technology, London, UK, Technical (Scientific) Note No. 10, December 1961.
45. M. H. Keegan, D. Nash, and M. Stack. **Numerical modelling of hailstone impact on the leading edge of a wind turbine blade**, in *Proc. EWEA Annual Wind Energy Event*, Vienna, Austria, February 2013.
46. E. M. Schulson. **Brittle failure of ice**, *Engineering Fracture Mechanics*, Vol. 68, pp. 1839-1887, December 2001.